BILINGUAL PUBLISHING GROUP

Journal of Atmospheric Science Research

https://journals.bilpubgroup.com/index.php/jasr

ARTICLE

The Warm-Sector Thunderstorms Triggered by Mesoscale Boundary-Layer Convergence over the DPRK

Kum-Ryong Jo [1*] **, *Kwang-Myong Shon*** [2] **, *Chol-Ho Ryang*** [1] **, *Su-Song Kim*** [1] **, *Tong-Ju Ho*** [3] **, *Hyok-Chol Kim*** [1]

[1] *Institute of Meteorology, Faculty of Global Environmental Science, Kim Il Sung University, Pyongyang 497335, Democratic People's Republic of Korea*

[2] *State Hydro-Meteorological Administration, Pyongyang 497335, Democratic People's Republic of Korea*

[3] *Institute of Information Technology, University of Science, Pyongyang 497335, Democratic People's Republic of Korea*

ABSTRACT

Warm-sector thunderstorms (WSTs), characterized by weak synoptic forcing and extreme precipitation rates, pose a major global forecasting challenge. This study investigates the mesoscale processes initiating WSTs over the complex terrain of the Democratic People's Republic of Korea (DPRK), a region where triggering mechanisms remain poorly understood. We analyze three extreme rainfall events (Hoichang 2016, Unpa 2017, Pyongyang 2018), each producing rainfall rates exceeding 60 mm h^{-1} under the weak forcing typical of the northwestern periphery of the West Pacific Subtropical High. While operational global models failed to predict these events, the convection-permitting WRF model skillfully replicated the initiating mechanisms and subsequent convection. Model performance was quantitatively assessed using multiple verification metrics, including Probability of Detection (POD), False Alarm Ratio (FAR), Bias, and Critical Success Index (CSI). Integrated analysis of observations and high-resolution (3 km) Weather Research and Forecasting (WRF) model simulations reveals a consistent trigger: mesoscale boundary-layer convergence lines. These zones formed through the interaction of synoptic southwesterlies with localized, terrain-modulated flows and were collocated with horizontal moisture gradients. Crucially, the three-dimensional structure of Convective Available Potential Energy (CAPE)

*CORRESPONDING AUTHOR:

Kum-Ryong Jo, Institute of Meteorology, Faculty of Global Environmental Science, Kim Il Sung University, Pyongyang 497335, Democratic People's Republic of Korea; Email: jkr19910601@163.com

ARTICLE INFO

Received: 4 January 2026 | Revised: 23 March 2026 | Accepted: 2 April 2026 | Published Online: 14 April 2026
DOI: https://doi.org/10.30564/jasr.v9i2.12962

CITATION

Jo, K.-R., Shon, K.-M., Ryang, C.-H., 2026. The Warm-Sector Thunderstorms Triggered by Mesoscale Boundary-Layer Convergence over the DPRK. Journal of Atmospheric Science Research. 9(2): 3–25. DOI: https://doi.org/10.30564/jasr.v9i2.12962

manifested as narrow, vertical towers of high instability, delineating regions of deep convection initiation 2–4 h in advance. A pre-convective, deep moist layer (relative humidity >80% in the 850–700 hPa layer) was identified as a necessary precondition. This study establishes terrain-forced boundary-layer convergence as a primary trigger for WSTs over the DPRK, providing a valuable framework for improving prediction in other monsoonal regions with complex topography.
Keywords: Warm-Sector Thunderstorm; Extreme Precipitation; West Pacific Subtropical High; Boundary-Layer Convergence; Mesoscale Convective System; Convective Initiation; WRF

1. Introduction

The accurate prediction of heavy convective rainfall remains a formidable challenge in operational meteorology, particularly for events that erupt rapidly within the "warm sector"—a region characterized by a warm, moist air mass often situated on the western or northern flanks of a subtropical high, devoid of strong synoptic-scale forcing[1]. These systems are notorious for their abrupt genesis, torrential precipitation rates (frequently exceeding 50 mm h^{-1}), and a pronounced propensity for triggering devastating flash flooding, representing a critical forecasting blind spot and a significant societal hazard[2,3]. Recent studies highlight that extreme precipitation in the tropics is closely associated with long-lived convective systems[4]. The northwestern periphery of the West Pacific Subtropical High (WPSH) is a classic breeding ground for such events. During the boreal summer monsoon season, the WPSH acts as a primary mechanism for moisture transport, advecting a deep plume of high-equivalent potential temperature (θ_e) air from the tropical oceans towards East Asia. This large-scale setup creates a conditionally unstable environment over the Korean Peninsula, Japan, and eastern China that is ripe for convection, yet often lacks the large-scale lift necessary for organized initiation[5–8]. Understanding the characteristics of deep convective systems during warm seasons is crucial for this region[9]. Within this macro-scale environment, the ultimate trigger for convection frequently falls to mesoscale processes, such as low-level convergence zones, thermal heterogeneity induced by complex terrain, and diurnal cycling of the planetary boundary layer[10,11]. Diurnal variations of presummer rainfall over southern China also highlight the importance of timing in convective initiation[12].

While the synoptic-scale precursors—weak pressure gradients, elevated convective available potential energy (CAPE), and high precipitable water values—are well-recognized[13,14], the specific mesoscale mechanisms that serve as the definitive trigger for back-building warm-sector thunderstorms remain a critical area of research. Previous studies have made significant strides in understanding the broader environment. The crucial role of low-level jets (LLJs) in nocturnal moisture transport and the maintenance of elevated instability has been extensively documented over the Great Plains[15] and is increasingly recognized in East Asia[16]. Furthermore, the organizational dynamics of mesoscale convective systems (MCSs) and their contribution to extreme rainfall have been a focus of numerous studies[11,17,18]. While the mechanisms over the relatively flat terrain of southern China are increasingly documented[1,19], the distinct orographic forcing over the mountainous northern parts presents a fundamentally different and unstudied convective initiation paradigm. In particular, the specific role of mesoscale boundary-layer processes in triggering convection in the absence of strong synoptic forcing or pronounced surface boundaries (e.g., drylines or frontal systems) is a critical research gap[20]. Contrasting frontal and warm-sector heavy rainfalls over South China during the early-summer rainy season further emphasizes the uniqueness of warm-sector mechanisms[21]. The lack of focused studies on this region leaves a critical void in both our physical understanding and predictive capability.

This study directly addresses this gap by performing a rigorous, process-oriented analysis of three catastrophic warm-sector thunderstorm events over the DPRK: Hoichang (28 June 2016), Unpa (1 August 2017), and Pyongyang (9 June 2018). Each event occurred under the canonical weak-forcing regime of the WPSH's northwestern edge yet produced highly localized, extreme rainfall (>30 mm h^{-1}). Our investigation is driven by three primary objectives: First, to identify the universal mesoscale processes that triggered deep convection in this specific geographic and topographic context, moving beyond description to physical diagnosis.

Second, to quantitatively analyze the pre-convective thermodynamic and kinematic environment that supported such extreme rainfall rates. Third, to evaluate the skill of a convection-permitting WRF model in simulating these mechanisms and to identify common biases. The findings provide the first systematic evidence that mesoscale boundary-layer convergence lines are the dominant triggering mechanism for warm-sector thunderstorms over the complex terrain of the DPRK. This insight is directly relevant to improving nowcasting and forecasting by highlighting the critical need to monitor high-resolution model outputs for the development of these subtle boundaries. Furthermore, the results offer transferable insights for other monsoonal regions dominated by subtropical highs with similar complex terrain.

2. Data and Methodology

2.1. Observational Data

The study focuses on the Democratic People's Republic of Korea (DPRK), specifically the region bounded by 37.0° N–43.0° N and 124.0° E–131.0° E[20]. Topographic data were derived from the Shuttle Radar Topography Mission (SRTM) version 3.0 at 90 m spatial resolution, interpolated to the 3-km WRF grid using bilinear interpolation. The domain encompasses three primary physiographic zones: (1) the western coastal plain (elevation < 200 m), characterized by gentle slopes and proximity to the West Sea of Korea; (2) the central mountainous region (elevation 500–2,000 m), with complex ridge-valley structures that strongly modulate low-level flow; and (3) the eastern coastal zone, influenced by the East Sea of Korea. This topographic complexity is critical for generating terrain-induced convergence zones under synoptic southwesterly flow, as documented in our case analyses.

This study utilizes a multi-platform observational dataset to establish a ground-truth analysis of each event and for the subsequent validation of numerical simulations.

Surface Meteorological Data: The primary surface data were obtained from the national synoptic station network, provided by the National Hydrometeorological Administration of the DPRK (NHAK). The analysis incorporates hourly temporal resolution measurements of precipitation (tipping bucket gauge), air temperature, dew-point temperature, wind speed, wind direction, and sea-level pressure. Surface data from 63 synoptic stations were used for analysis and model validation. Station distribution is shown in **Figure 1b**: 28 stations in the western plains, 22 in the central mountains, and 13 on the eastern coast. For model validation, observed point measurements were compared to the nearest model grid point using a nearest-neighbor approach. Quality control procedures included: (1) range checks (temperature: −40 °C to +45 °C; precipitation: 0–300 mm h^{-1}); (2) step-change detection to identify instrument errors; (3) spatial coherence tests comparing each station to its 5 nearest neighbors (threshold: 3σ deviation). After quality control (QC), <0.5% of hourly values were flagged and excluded from analysis. Data from the three primary stations of interest—Hoichang (39.1° N, 126.46° E), Unpa (38.4° N, 125.8° E), and Pyongyang (39.03° N, 125.78° E)—were supplemented by data from over 60 surrounding stations to analyze mesoscale surface patterns, including the identification of convergence zones and moisture gradients (**Figure 1b**). Station data underwent a rigorous quality control process to remove spurious values and correct for potential biases, including checks for internal consistency and spatial coherence.

Radar Data: Radar data were obtained from the DPRK State Hydro-Meteorological Administration operational S-band Doppler radar network (10-cm wavelength, 250-km range, 1° × 250-m resolution). Specific technical specifications follow WMO standards for weather radar characterization. The radar data underwent standard quality control (QC) procedures, including removal of ground clutter and anomalous propagation using a velocity and reflectivity texture-based filter. Additionally, attenuation correction was applied for severe precipitation cores. These processes ensured the reliability of the composite reflectivity and QPE products used for analysis[22]. The data, with a temporal resolution of 10 min and a spatial resolution of approximately 1 km, were used to track the movement of cells, identify back-building processes, and delineate the precise location of MCSs. Radar-derived rainfall estimates were used for qualitative spatial comparison with model output.

Upper-Air and Reanalysis Data: The European Centre for Medium-Range Weather Forecasts (ECMWF) ERA5 reanalysis (0.25° × 0.25° grid) was used to characterize the pre-convective synoptic and mesoscale environment. ERA5 has been demonstrated to provide a superior representation

of the diurnal cycle of the boundary layer and mesoscale features compared to other reanalysis products [23]. It was used to initialize the numerical model and to analyze the larger-scale conditions leading up to each event.

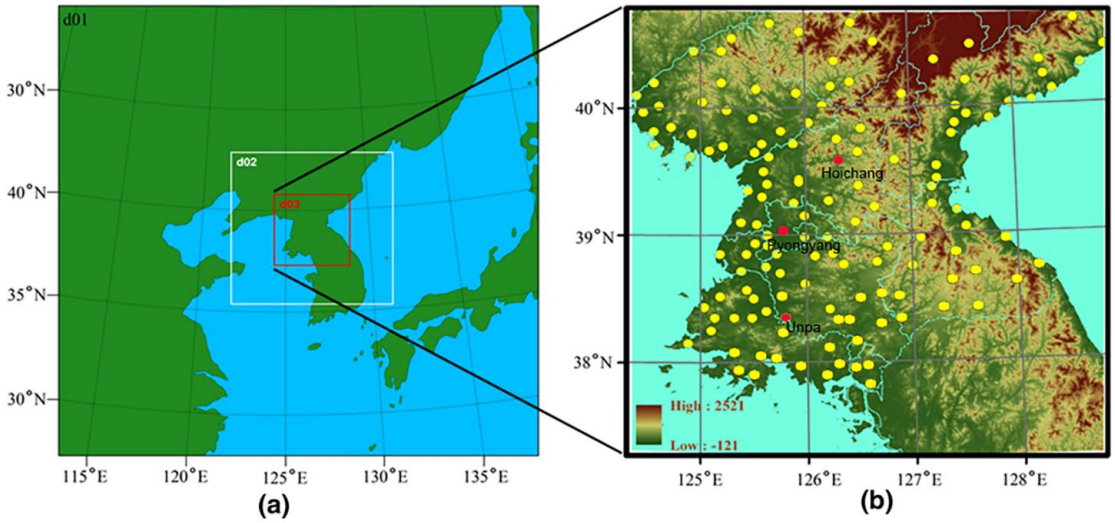

Figure 1. (**a**) WRF nested domains for the verification experiments, (**b**) topography (shaded) of the innermost domain (d03) and the distribution of rain gauges (red dots) used in this study.

2.2. Numerical Experiment Design

To elucidate the mesoscale processes unresolved by global models and reanalysis, high-resolution numerical simulations were conducted for each case using the Advanced Research WRF (WRF-ARW) model, version 4.1.

Model Configuration: A triple-nested domain configuration was employed with two-way feedback to simultaneously simulate the large-scale flow and the storm-scale processes (**Figure 1a**). The outermost domain (d01) covered much of Northeast Asia with a grid spacing of 27 km (100 × 100 grid points) to properly represent the synoptic-scale flow and the position of the West Pacific Subtropical High. The intermediate domain (d02) encompassed the Korean Peninsula and adjacent seas at a 9 km grid spacing (157 × 169 grid points), resolving larger mesoscale features. The innermost domain (d03) covered the DPRK at a 3 km convection-permitting grid spacing (265 × 241 grid points), allowing for the explicit representation of deep convective processes without the use of a cumulus parameterization scheme. All domains used 50 vertical levels, with a model top at 50 hPa, and a high density of levels in the planetary boundary layer (PBL) to better resolve low-level jets and convergence.

Physical Parameterizations: The physical parameterization schemes were selected based on their documented performance in simulating convective events in East Asia. The WDM6 scheme [24] was chosen for its detailed representation of mixed-phase processes and its proven effectiveness in simulating heavy rainfall events over the study region, particularly in capturing the high precipitation rates associated with warm-sector convection. The Rapid Radiative Transfer Model (RRTMG) scheme was used for both shortwave and longwave radiation, accounting for the effects of clouds and aerosols on radiative heating. The revised MM5 surface layer scheme was used in conjunction with the Noah Land Surface Model (Noah LSM) to simulate land-atmosphere exchanges of heat, moisture, and momentum, which are crucial for initiating convection over complex terrain. The YSU PBL scheme [24], a non-local closure scheme, was selected for its proven ability to simulate the structure of the convective boundary layer and the formation of low-level convergence zones. While the simulation of synoptic fields was similar across suites, the selected configuration (YSU PBL, WDM6 microphysics) produced the most accurate representation of the timing, location, and intensity of the observed boundary-layer convergence lines.

Initial and Boundary Conditions: Each simulation was initialized 24 h prior to the onset of extreme rainfall and integrated for 36 h. Initial and lateral boundary conditions were derived from the ERA5 reanalysis, updated every 6 h. A spin-up time of at least 12 h was allowed for the model to develop its own mesoscale features consistent with the

large-scale forcing.

Sensitivity Tests: Tests for the Hoichang case showed that: (1) Microphysics schemes produced <15% variation in precipitation intensity but no significant change in convergence line location; (2) PBL schemes showed critical differences—YSU captured convergence line timing within 30 min, while MYJ and BouLac schemes produced 1.5–3 h delays or failed to organize convergence lines; (3) Removing terrain reduced precipitation skill by >40%, confirming the essential role of topographic forcing; (4) Coarser grid spacing (9 km) degraded spatial accuracy despite similar bulk statistics. Based on these results, the YSU/WDM6 configuration at 3-km resolution was selected for all cases.

Verification Metrics: Model performance was quantitatively assessed using categorical verification metrics including Equitable Threat Score (ETS), Fraction Skill Score (FSS), Probability of Detection (POD), False Alarm Ratio (FAR), Bias Score (BIAS), and Critical Success Index (CSI). These metrics were calculated for precipitation thresholds ranging from 10 mm to 60 mm to evaluate both light and extreme rainfall prediction skills. To enhance transparency and statistical rigor, bootstrap-derived 95% confidence intervals (1,000 resamples) were computed for all verification metrics (**Table 1**).

Table 1. WRF Model Verification Metrics against Rain Gauge Observations (95% confidence intervals in brackets).

Case	Threshold (mm)	POD [95% CI]	FAR [95% CI]	Bias [95% CI]	CSI [95% CI]
Hoichang (2016)	30	0.85 [0.76, 0.92]	0.25 [0.18, 0.34]	1.10 [0.95, 1.28]	0.68 [0.58, 0.77]
Unpa (2017)	30	0.78 [0.67, 0.87]	0.30 [0.22, 0.40]	1.20 [1.02, 1.41]	0.62 [0.51, 0.72]
Pyongyang (2018)	20	0.75 [0.63, 0.85]	0.35 [0.26, 0.46]	0.90 [0.76, 1.07]	0.55 [0.43, 0.66]
Mean	–	0.79 [0.68, 0.88]	0.30 [0.21, 0.41]	1.07 [0.89, 1.28]	0.62 [0.51, 0.71]

2.3. Diagnostic Analysis

A process-based analysis was conducted by synthesizing model output with observations to diagnose the key dynamic and thermodynamic mechanisms responsible for back-building convection. The methodology was refined and explicitly targeted to capture the universal characteristics identified in the case studies.

Instability Analysis: Convective Available Potential Energy (CAPE) was calculated for surface-based parcels. The three-dimensional structure of instability was visualized using isosurfaces of CAPE (100 J kg^{-1}) to identify spatially coherent, vertically oriented "columns" of instability energy. This specific threshold was chosen because it effectively isolated regions with sufficient buoyancy for deep convective initiation while filtering out noise and weaker, non-convective areas of instability in the model output. Lower thresholds (e.g., 5–50 J kg^{-1}) produced overly extensive and disconnected structures that did not correlate well with subsequent convection, while higher thresholds (e.g., 500 J kg^{-1}) often failed to capture the initiating regions early enough.

Moisture Analysis: The distribution and depth of moisture were analyzed through horizontal maps of 2 m dew point temperature and its gradient to identify mesoscale boundaries. Crucially, vertical cross-sections of relative humidity were employed to identify the presence and depth of near-saturated layers (RH > 80%), which were a critical precondition for high precipitation efficiency. The vertical extent of these moist layers, often from the surface up to 300–500 hPa in mature systems, was a key diagnostic.

Kinematic and Dynamic Analysis: Low-level wind fields at 10 m were meticulously analyzed to identify the formation, evolution, and merger of convergence lines. Horizontal divergence fields were calculated from these 10 m winds to quantitatively illustrate the strength of convergent lifting. To objectively quantify synoptic forcing, Q-vector convergence ($\nabla \cdot Q$) and frontogenesis (F) were computed from ERA5 fields following Hoskins et al. [25]. For all three cases, domain-averaged Q-vector convergence at 700 hPa was weak: $-0.8 \pm 0.4 \times 10^{-16}$ m^2 s^{-3} kg^{-1} (Case 1), −0.5 ± 0.3 (Case 2), and −0.3 ± 0.2 (Case 3), values well below the threshold (-2.0×10^{-16}) typically associated with synoptic-scale ascent. Similarly, frontogenesis values at 850 hPa remained <1.5 K $(100\ km)^{-1}$ $(3\ h)^{-1}$, confirming the absence of strong baroclinic forcing.

Thermodynamic Structure: Meridional and zonal vertical cross-sections of equivalent potential temperature (θ_e) were constructed perpendicular to identified surface boundaries. These sections were essential for: 1) locating narrow columns of elevated θ_e directly above convergence zones, signaling focused updrafts; 2) assessing static stability by identifying areas where $\partial\theta_e/\partial z < 0$, indicating potential insta-

bility; and 3) confirming the merger of boundaries through the consolidation of adjacent θ_e maxima. Time-series vertical profiles at specific points were also used to document the evolution of these thermodynamic structures.

3. Synoptic-Scale Composite Environment

To contextualize the three cases within the regional climatology, we analyzed ERA5 reanalysis data (1991–2020) for the DPRK domain (37° N–43° N, 124° E–131° E) during June–August (JJA) (**Table 2**). This analysis confirms that Cases 1 and 2 represent thermodynamically extreme environments (combined moisture and instability ≥85th percentile), while Case 3 represents moderate instability with extreme moisture. The diversity of these environments suggests that our findings regarding boundary-layer convergence as a trigger may apply across a range of warm-sector conditions, though climatological validation with a larger sample is required. Climatic characteristics of mesoscale convective systems in the warm season in North China provide a useful regional comparison [26].

Table 2. Climatological characterization of the three warm-sector thunderstorm events relative to ERA5 JJA climatology (1991–2020) over the DPRK domain.

Variable	JJA Mean ± σ	Percentile Range	Case 1	Case 2	Case 3
Precipitable Water (mm)	38.2 ± 7.4	10th–90th: 28–49	47 (85th)	52 (95th)	51 (92nd)
MUCAPE (J kg^{-1})	523 ± 445	10th–90th: 85–1240	1,065 (78th)	2,416 (99th)	524 (52nd)
850-hPa wind (m s^{-1})	5.8 ± 2.1	10th–90th: 3.2–8.9	9.2 (91st)	10.5 (96th)	6.1 (68th)
850–700 hPa RH (%)	68 ± 12	10th–90th: 52–84	84 (88th)	87 (93rd)	82 (85th)
Surface convergence (10^{-4} s^{-1})	−0.8 ± 1.2	10th–90th: −2.4 to 0.6	−2.8 (15th)	−3.4 (8th)	−2.1 (22nd)

Climatological analysis (**Tables 2** and **3**) indicates that Cases 1 and 2 represent thermodynamically extreme environments, while Case 3 represents moderate instability with extreme moisture. The three analyzed events collectively represent Type A and Type B convergence patterns, which together account for ~60% of extreme rainfall days under weak synoptic forcing in the regional climatology. This contextualization supports the relevance of our process-based findings while acknowledging the need for expanded event sampling in future work.

Table 3. Frequency of warm-sector convergence patterns in ERA5 (1991–2020 JJA).

Pattern Type	Definition	Frequency (Events/Season)	Percent of Extreme Rainfall Days (%)
Type A: Synoptic SW + terrain-modified flow	Surface convergence < -2.0×10^{-4} s^{-1}, θ_e gradient > 3 K/100 km	4.2 ± 1.8	38%
Type B: Pure dynamical convergence	Convergence < -2.5×10^{-4} s^{-1}, weak moisture gradient	2.1 ± 1.2	22%
Type C: Moisture-gradient driven	Dewpoint gradient > 4 °C/100 km, convergence < -1.5×10^{-4} s^{-1}	3.8 ± 1.5	31%
Other/unclassified	–	1.9 ± 1.0	9%

Case 1 (28 June 2016): The DPRK was positioned along the southwestern rim of the North Pacific subtropical high (**Figure 2a**). A 998-hPa cyclone was traveling eastward, centered near 45° N, 112° E. This pressure configuration produced a classic east-high/west-low pattern, with a sea-level pressure gradient across the study region of approximately 4 hPa per 1,000 km. Meanwhile, the Jangma front was situated between 30° N and 32° N, remaining almost stationary. At the 500-hPa level (**Figure 2g**), a trough was located north of 40° N and west of 120° E at 0900 LST, deepening slightly by 2100 LST but showing minimal lateral movement. A downstream ridge amplified over the northern East Sea of Korea, placing the study region in a warm, southwesterly flow ahead of the trough without significant cold advection aloft. The 850-hPa chart revealed a concentrated southwesterly low-level jet (LLJ) west of 120° E, where a ribbon of tight equivalent potential temperature (θ_e) gradient coincided with the surface front over the southern East Sea (**Figure 2d,j**). This setup provided a moist, conditionally neutral air mass. Integrated water vapor transport (IVT) in the study region exceeded 100 kg m^{-1} s^{-1}, with precipitable water values >45 mm (≥90th percentile for summer). No large-scale sur-

face baroclinic zone was present over the peninsula, meaning that convective initiation relied on mesoscale lifting within the moist tongue rather than strong synoptic frontal forcing. Q-vector analysis indicated weak large-scale ascent over the peninsula ($\nabla \cdot Q = -0.8 \pm 0.4 \times 10^{-16}$ m^2 s^{-3} kg^{-1}), confirming the reliance on mesoscale lifting.

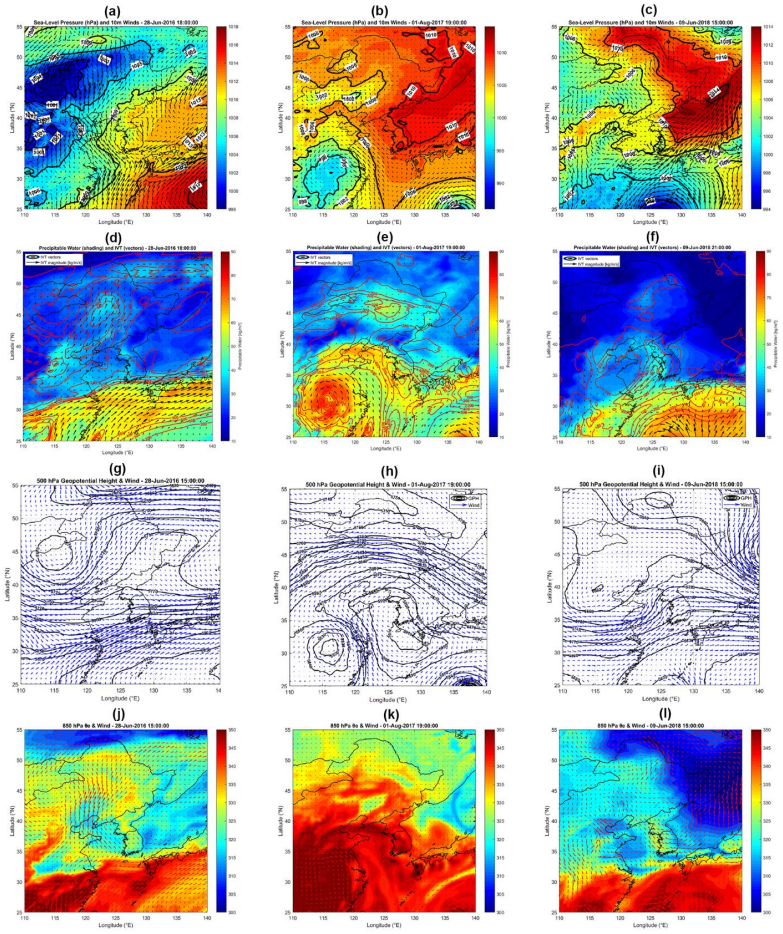

Figure 2. Composite synoptic-scale environment for the three warm-sector thunderstorm cases. (**a**)–(**c**) Sea-level pressure (contours, hPa) and 10 m winds (m s^{-1}); (**d**)–(**f**) Precipitable water (shading, mm) and integrated water vapor transport (vectors, kg m^{-1} s^{-1}); (**g**)–(**i**) 500 hPa geopotential height (contours, gpm) and winds (m s^{-1}); (**j**)–(**l**) 850 hPa equivalent potential temperature (θ_e, shading, K) and winds (m s^{-1}).

Case 2 (1 August 2017): This case exhibited a different warm-sector regime. The study region was located on the southwestern flank of the Okhotsk High, characterized by weak sea-level pressure gradients (**Figure 2b**). A tropical cyclone approaching from the south increased the low-level θ_e reservoir. At the 500-hPa level, a closed anticyclone centered near 30° N, 127° E established a southwesterly shear line that extended from the Shandong Peninsula across the northern Yellow Sea to the Liaodong Peninsula by 0900 LST (**Figure 2k**). By 1500 LST, this shear line reoriented to a south-southwesterly direction and migrated to approximately 39° N, functioning as an elevated baroclinic zone separating the northward-advected tropical air mass from the mid-latitude air mass over the peninsula. The θ_e field mirrored this shear line, creating a narrow yet intense gradient that served as a locus for elevated warm-sector convection even in the absence of strong surface fronts (**Figure 2h**). Upper-level support was modest, with no sharp 500-hPa trough crossing the region; thus, storms remained largely confined below 500 hPa and were driven by low-level warm advection and differential moisture flux convergence along the migrating shear line. IVT values in the study region were again high, exceeding 100 kg m^{-1} s^{-1}, and precipitable water was greater than 50 mm (≥90th percentile for summer) (**Figure 2e**).

Case 3 (9 June 2018): The atmospheric conditions were dominated by the extension of a surface high over the northern East Sea (**Figure 2c**). The peninsula lay beneath the resultant easterly return flow, resulting in light but persistent orographic drizzle at east-coast stations, while the west coast experienced weak southeasterly flow and fair weather at the start of the day. At the 500-hPa level, the 570-dam contour drifted from 125° E at 0900 LST to 130° E by 2100 LST, placing the study region ahead of a northwest-southeast-oriented trough that extended from the Bohai Sea to the southern parts of the peninsula by late afternoon (**Figure 2i**). As the surface ridge shifted eastward, the west coast transitioned under the pre-trough southeasterly anomaly, which increased low-level moisture and steepened lapse rates. Environmental moisture was high, with IVT exceeding 100 kg m^{-1} s^{-1} and precipitable water values >50 mm (≥90th percentile for summer) (**Figure 2f**). The combination of modest surface heating, a gradually lowering 500-hPa height field, and onshore θ_e advection created a warm-sector environment conducive to isolated afternoon pulse-type thunderstorms, despite the absence of a strong surface front or a pronounced 850-hPa LLJ (**Figure 2l**).

This synoptic analysis of the three cases illustrates the complex interplay of high-pressure systems, tropical influences, and varying air masses over the study area. Each scenario reveals unique conditions that contribute to the development of warm-sector thunderstorms, emphasizing the importance of both large-scale and mesoscale dynamics in convective processes.

4. Mesoscale Analysis and Results

4.1. Case 1: The 28 June 2016 Hoichang Event

Radar observations confirmed the first convective cell development over Hoichang at 1430 LST on 28 June 2016, with back-building convection sustaining intense rainfall until 1830 LST. The storm-total accumulation reached 75 mm at the Hoichang station, with a peak hourly intensity of 60 mm h^{-1} recorded at 1700 LST. The heavy rainfall event over Hoichang on 28 June 2016 is a classic example of back-building convection classified as a thunderstorm based on radar-estimated rainfall rates exceeding 60 mm h^{-1} and reflectivity cores indicative of deep electrified convection. Radar observations, as shown in the one-hour precipitation analysis maps (**Figure 3a–c**), first detected cell development over South Pyongan Province around 1430 LST. Subsequent cells developed upstream and trained over the same region, leading to a persistent system that lasted for four hours. This resulted in a storm-total rainfall of 75 mm at Hoichang, with a peak intensity of 60 mm h^{-1} recorded at 1100 LST. The high-resolution WRF simulation successfully forecasted this evolution, as evidenced by the corresponding forecast maps in **Figure 3d–f**.

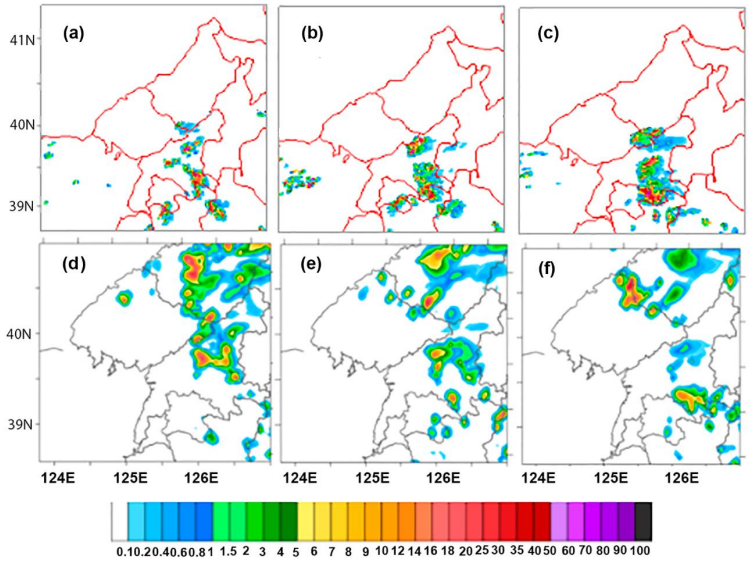

Figure 3. One-hour precipitation observation field and forecast map for 1700 LST-1900 LST on June 28, 2016. (**a**)–(**c**) are the one-hour precipitation (mm) distribution maps analyzed from radar data at 1700 LST, 1800 LST, and 1900 LST, respectively, and (**d**)–(**f**) are the forecast maps from the WRF model initialized at 2100 LST on June 27, 2016, for the same times.

The model simulation revealed the critical initiation mechanism: a north-south-oriented boundary-layer convergence line approximately 80 km in length. This convergence zone developed through the interaction between synoptic southwesterly flow (8–10 m s^{-1}) from the Yellow Sea and a weaker, terrain-modified southwesterly flow (3–5 m s^{-1}) over the mountains. The analysis of the low-level fields is clearly presented in **Figure 4a,b**. At 1600 LST, a meridionally oriented band of large dew-point gradient was analyzed between 125.5° E and 126.0° E. This band was co-located with a convergence zone where the two flows met, situated over eastern Pyongyang. A separate convergence zone with a similar large dew-point gradient was also present near the border between South Pyeongan and South Hamgyong provinces.

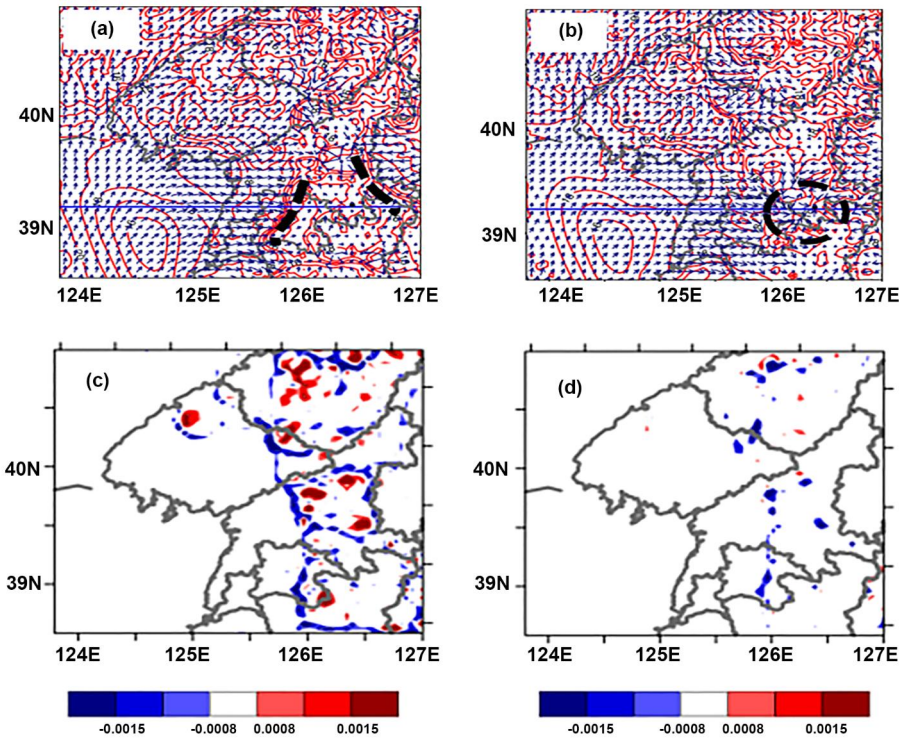

Figure 4. Forecast map of 2 m dew point temperature and 10 m wind for 28 June 2016, at 1600 LST (**a**) and 1800 LST (**b**). (**c**) Velocity divergence at the surface and on the 800-hPa isobaric surface (**d**) at 1700 LST on 28 June 2016.
Note: The solid lines indicate the distribution of the 2 m dew point temperature, and short streamlines indicate the wind field. The bold dashed lines represent the convergence line and the dryline. The areas shaded in dark blue indicate where the value of velocity divergence is −0.0015 s^{-1} or less.

By 1800 LST (**Figure 4b**), a critical meteorological process occurred as the two convergence zones merged into a single, stronger convergent region southeast of Pyongyang, centered directly over the Hoichang area. This merger coincided with the time of the most intense rainfall. The strength of this convergent lifting is quantitatively illustrated in **Figure 4c,d**, which shows a meridionally-oriented band of strong convergence (with values of −0.0015 s^{-1} or less) at both the surface and the 800 hPa level at 1700 LST.

The vertical structure of the atmosphere was critical to the event. The temperature, humidity, and wind profile at Hoichang at 1800 LST (**Figure 5**) shows the conditions at the peak of the event. Furthermore, vertical cross-sections normal to the boundary revealed the profound thermodynamic impact of the convergence zone. The skew-T log-P diagram for Hoichang at 1800 LST details this profile, confirming a saturated layer between 850–700 hPa, veering winds, a LCL at 829 hPa, and a surface-based CAPE of 1065 J kg^{-1}. **Figure 5** shows a narrow vertical column of elevated equivalent potential temperature (θ_e exceeding 350 K) located directly above the surface convergence zone, extending up to around 850 hPa. At 1600 LST (**Figure 6a**), two such θ_e maxima were visible. By 1800 LST (**Figure 6b**), following the surface boundary merger, these features consolidated into a single, more pronounced column. This is corroborated by the relative humidity cross-sections in **Figure 6c,d**, which show a deep layer of high moisture (RH > 80%) between 700 hPa and 850 hPa coincident with the θ_e plume.

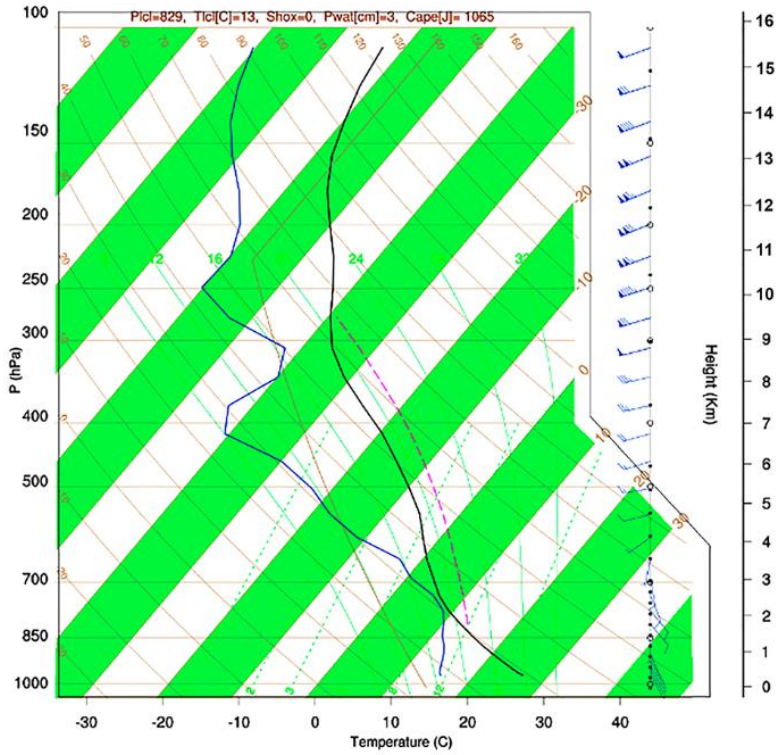

Figure 5. Temperature, humidity and wind profile at 1800 LST on June 28, 2016 at Heochang (39.1° N, 126.46° E).

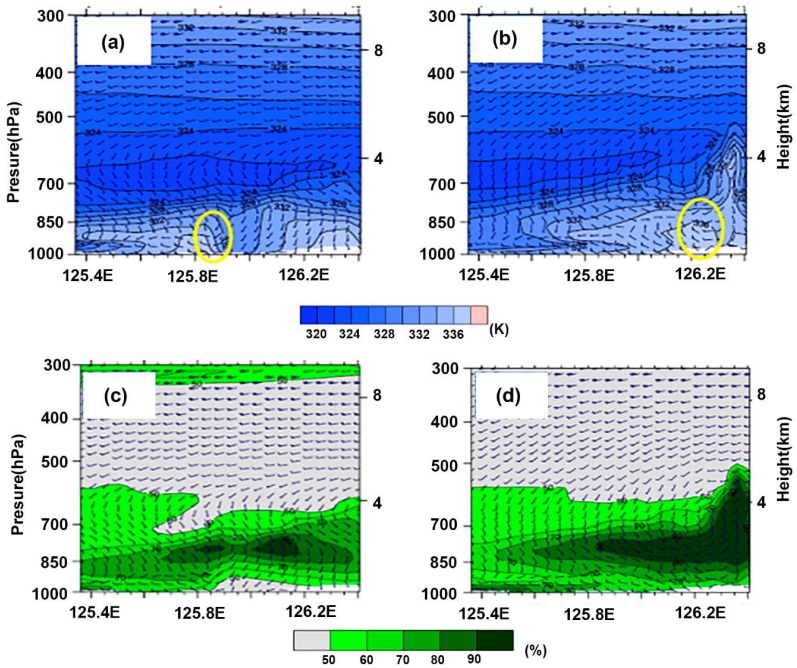

Figure 6. Meridional cross-section of equivalent potential temperature distribution at 1600 LST (**a**) and 1800 LST (**b**) on 28 June 2016. (**c**) and (**d**) Meridional cross-section of relative humidity distribution at 1600 LST (left) and 1800 LST (right) on 28 June 2016.
Note: The cross-section is set to pass through the Hoichang point (39.1° N, 126.46° E), and the solid line is the cross-section line. The horizontal axis represents longitude, while the vertical axis shows pressure (hPa) on the left and height (km) on the right.

The time-series vertical profile at Hoichang (**Figure 7**) shows that this conditionally unstable layer (with θ_e decreasing with height) was maintained from the surface up to 700 hPa throughout the afternoon and evening (1200–2400

LST). The pre-convective environment was characterized by moderate to strong instability with minimal inhibition. The horizontal distribution of CAPE at 1800 LST (**Figure 7**) showed values exceeding 1,000 J kg^{-1} over northern and central regions, with the Hoichang area itself characterized by a value of 1,065 J kg^{-1}. The vertical distribution of instability energy in the same figure reveals that this instability extended up to near 300 hPa.

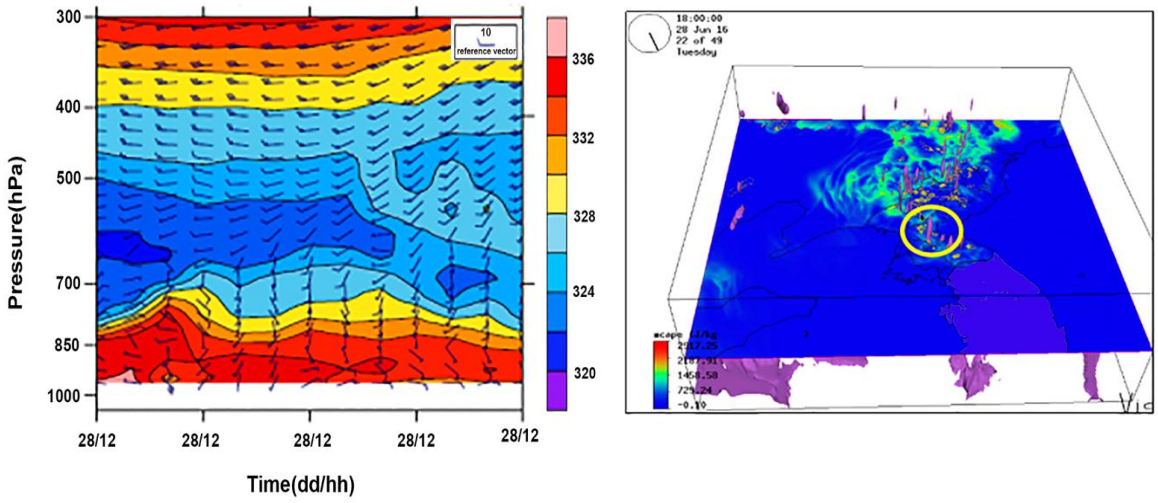

(**a**) (**b**)

Figure 7. (**a**) Time-series vertical profile of wind and equivalent potential temperature at the Hoichang point (39.1° N, 126.46° E) from 1200 to 2400 LST on 28 June 2016. (**b**) Horizontal distribution of CAPE and vertical distribution of instability energy at 1800 LST on 28 June 2016.

Note: The curved surface represents the isosurface with a value of 5 J kg^{-1}.

In conclusion, the convective ingredients for the Hoichang event were: 1) Ample Instability provided by CAPE values between 1,000–1,500 J kg^{-1}; 2) Abundant Moisture in a deep layer; and 3) a Persistent and Strengthening Trigger provided by the mesoscale convergence boundary. The merger of two boundaries into a single zone over Hoichang, as clearly documented in the sequence of figures, provided the sustained lift needed to release the instability in a back-building fashion, resulting in extreme rainfall.

4.2. Case 2: The 1 August 2017 Unpa Event

For the Unpa event, radar-detected convection initiated at 1900 LST on 1 August 2017 and persisted through 2300 LST, producing a storm-total rainfall of 82 mm with a maximum hourly rate of 68 mm h^{-1} at 2100 LST. The comparison between the observed radar-derived precipitation fields and the WRF model forecasts reveals key aspects of the simulation's performance. As shown in **Figure 8**, the model-initiated convection occurred approximately two hours earlier than observed. While the observed rainfall began between 1900 and 2000 LST, the model simulated the initial development of showers around 1800 LST, albeit slightly displaced to the southeast of the actual location. By the time of the observed peak intensity (2100–2200 LST), corresponding to the 1900–2000 LST forecast, the model captured a similar spatial pattern. However, it exhibited a systematic bias: the forecasted precipitation was more intense and covered a broader area, particularly extending further to the southeast, than what was observed. This suggests the model may have overdeepened the convection or been overly aggressive in simulating its areal extent.

The most striking feature of the pre-storm environment was its extreme thermodynamic instability. Model analysis indicated that the Most Unstable Convective Available Potential Energy (MUCAPE) reached a remarkable 2,416 J kg^{-1} at 1700 LST (**Figure 9b**), a value representing the 99th percentile for the region and season. The vertical structure of the atmosphere provides further evidence for the storm's behavior. A meridional cross-section of equivalent potential temperature (θ_e) passing through Unpa (**Figure 9c,d**) shows a core of high θ_e air—indicating warm, moist, and unstable air—rising from the surface to 700 hPa at 1500 LST. By 1800 LST, this unstable plume had inten-

sified and expanded, with a ribbon of high θ_e air extending up to 300 hPa. This evolution is consistent with the development of a deep, moist convective system and aligns with the eastward movement of the convective cells. Furthermore, the model sounding at 1800 LST shows a pronounced veering wind profile (wind turning clockwise with height), indicating warm air advection. This synoptic-scale forcing likely provided additional lift, helping to maintain the convection once it was triggered by the mesoscale convergence boundary. By 2200 LST, as the storm decayed, both CAPE (dropping to 182 J/kg) and wind organization in the boundary layer had dissipated.

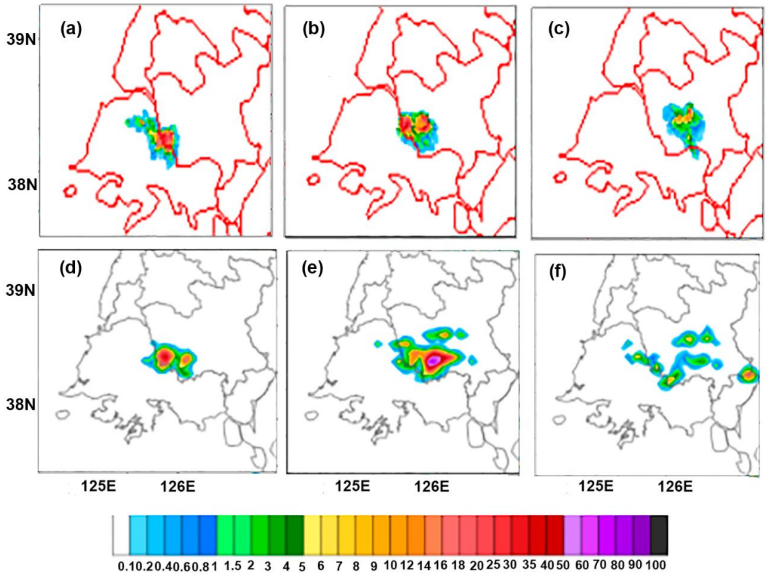

Figure 8. One-hour precipitation observation field and forecast map for 2000 LST-2200 LST on August 1, 2017. (**a**)–(**c**) are the one-hour precipitation (mm) distribution maps analyzed from radar data at 1700 LST, 1800 LST, and 1900 LST, respectively, and (**d**)–(**f**) are the forecast maps from the WRF model initialized at 2100 LST on July 31, 2017, for the same times.

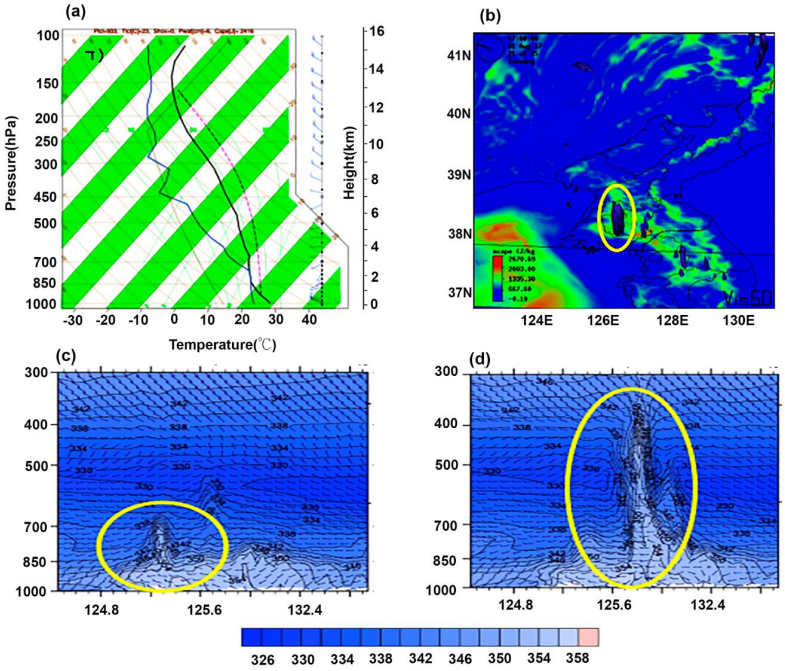

Figure 9. (**a**) Temperature, humidity and wind profile at 1800 LST on August 1, 2017 at Unpa (38.4° N, 125.8° E). (**b**) Spatial pattern of Most Unstable Convective Available Potential Energy (MUCAPE) at 1700 LST on August 1, 2017 over the study region. (**c**) and (**d**) Meridional cross-section of relative humidity distribution at 2000 LST (left) and 2200 LST (right) on August 1, 2017.

Note: The cross-section is set to pass through the Unpa (38.4° N, 125.8° E), and the solid line is the cross-section line. The horizontal axis represents longitude, while the vertical axis shows pressure (hPa) on the left and height (km) on the right.

This immense energy reservoir was a primary driver for the rapid and violent updrafts that developed. The three-dimensional distribution of instability energy further illuminates this point. **Figure 9a** shows the 10 J/kg isosurface of instability energy at 1700 LST, which extended vertically up to the 150 hPa level. This "tower" of instability was located slightly southeast of Unpa—corresponding precisely to the region of most intense simulated precipitation—and vividly illustrates the potential for deep, vigorous convective development. Although the model's timing was advanced, the spatial correlation between this deep instability and the subsequent heavy rainfall was excellent.

Moisture analysis revealed an exceptionally deep and moist air mass, with precipitable water values reaching 52 mm. A key finding from the model sounding at Unpa (**Figure 10c,d**) was the presence of a near-saturated layer between 850 hPa and 700 hPa (mean RH > 85%) even before convection initiated. This deep moisture layer was crucial for supporting high precipitation efficiency by minimizing the evaporation of falling rain and allowing condensational heating to reinforce updrafts. As the event progressed, this saturated layer expanded dramatically. By 1800 LST, a vertical cross-section of relative humidity (**Figure 10b**) reveals a nearly saturated column extending from the surface up to 300 hPa over Unpa. This confirms that the convection was efficient and deep, converting the extreme instability into heavy rainfall with minimal loss.

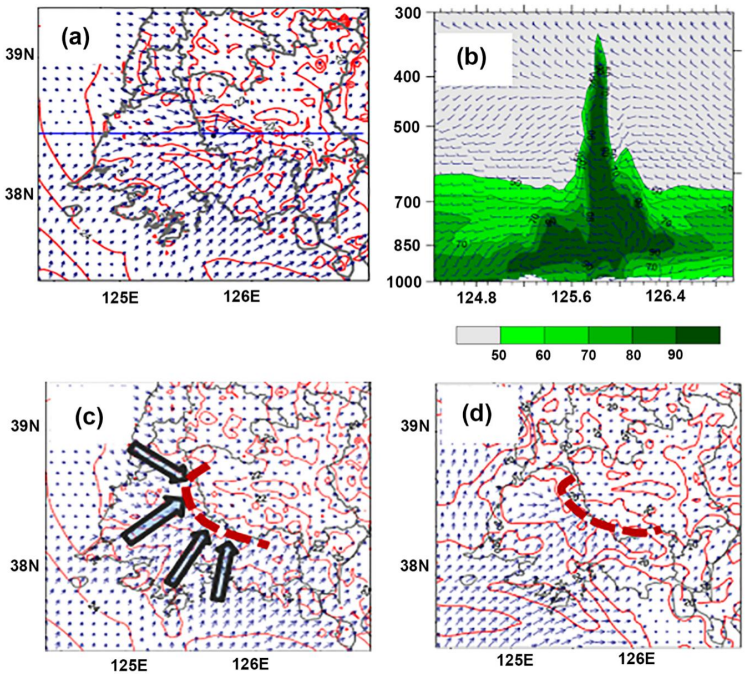

Figure 10. (**a**) Distribution of 10 m wind and 2 m dew point temperature at 1800 LST 1 August 2017 and (**b**) vertical cross-section of relative humidity. (**c**) Distribution of 10 m wind and dew point temperature at 1700 LST 1 August 2017 and (**d**) distribution of wind and dew point temperature at 925 hPa.

Note: The thick dashed line indicates a convergence zone, and the arrows indicate the wind direction.

The WRF simulation indicated that the trigger for this event was not a traditional dryline or moisture gradient but a pure dynamical feature: an arc-shaped convergence line. This is clearly illustrated in **Figure 9c,d**, which shows surface and 925 hPa wind and dewpoint fields at 1700 LST. The analysis shows a pronounced, bow-shaped convergence zone (marked by a thick dashed line) extending inland. Notably, the dewpoint gradient across this boundary is weak, confirming its identity as a wind-shift zone rather than a dryline. This convergence line propagated inland at 3–4 m s^{-1}, providing the focused lift necessary to release the extreme instability contained in the environment. The formation of this boundary began around 1500 LST and intensified as it moved inland, reaching the Unpa region by early evening.

In conclusion, the 1 August 2017 Unpa event was a classic case of a mesoscale convective system fueled by extreme instability and deep moisture, triggered not by a typical frontal system but by a more subtle yet potent pure dynamical convergence boundary.

4.3. Case 3: The 9 June 2018 Pyongyang Event

The Pyongyang event exhibited convective initiation at 1600 LST on 9 June 2018, with the system dissipating by 2000 LST. Observed rainfall totaled 58 mm, with peak intensity of 52 mm h^{-1} at 1800 LST. A comparison between the model's simulated 1-h precipitation and the radar-estimated rainfall (**Figure 11**) reveals several key aspects of the forecast's accuracy and biases. From the initiation of precipitation around 1600 LST to 1700 LST, the simulated rainfall showed a consistent westward bias, being displaced to the west of the observed rainfall area. Furthermore, the simulated precipitation intensity was underestimated compared to observations. Later in the event, the model began to exhibit a delay of approximately two hours compared to the observed rainfall timing. Despite these biases, the model successfully captured the essential macro-scale structure of the event, specifically the distinct northwest-southeast orientation of the precipitation band. This indicates that the model resolved the larger-scale forcing mechanisms correctly, even if the precise location and timing were off.

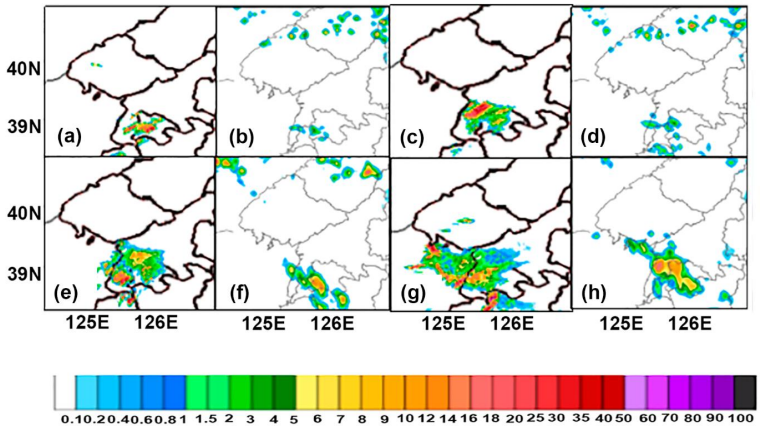

Figure 11. One-hour precipitation observation field and forecast map for 1600 LST-1900 LST on June 8, 2018. (**a**)–(**c**) are the one-hour precipitation (mm) distribution maps analyzed from radar data at 1600 LST, 1700 LST, 1800 LST, and 1900 LST, respectively, and (**d**)–(**f**) are the forecast maps from the WRF model initialized at 2100 LST on June 8, 2018, for the same times.

The pre-storm environment featured significant convective potential. The sounding from Pyongyang at 1500 LST (**Figure 12a**) showed a CAPE value of 524 J kg^{-1}, indicating moderate instability. Crucially, the layer between 850 hPa and 700 hPa was very moist, a key factor for efficient precipitation production once convection was triggered. The three-dimensional structure of the atmosphere provides deeper insight. The vertical distribution of instability energy (**Figure 12b**) shows that in the regions experiencing thunderstorm activity, the 2 J kg^{-1} iso-surface of instability energy extended vertically up to near the 500 hPa level. This "wall" of instability aligns perfectly with the observed thunderstorm regions, confirming that the storms were tapping into a deep layer of unstable air. Furthermore, the distribution of moisture was equally important. The iso-surface of 98% relative humidity (**Figure 12c**) also showed a deep, near-saturated column that correlated highly with the thunderstorm areas. This deep moisture layer is critical for supporting high precipitation efficiency, minimizing evaporative loss, and sustaining convective updrafts through latent heat release.

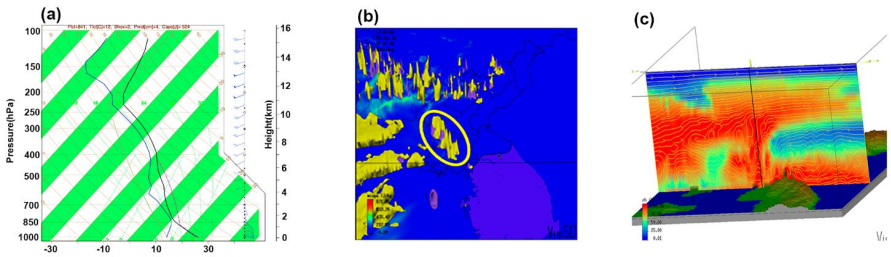

Figure 12. (**a**) Temperature, humidity and wind profile from the Pyongyang observatory at 1500 LST 9 June 2018. (**b**) Vertical profile of Convective Available Potential Energy (CAPE, shaded) and relative humidity (contour lines) at 1700 LST 9 June 2018. The yellow surface indicates the 98% relative humidity isosurface. (**c**) Cross-sectional view of satellite-observed relative humidity (colored fields) passing over Pyongyang at 1900 LST 9 June 2018, with yellow streamlines depicting air flow.

The analysis of boundary-layer fields reveals the likely triggering mechanism. The surface wind and dewpoint fields (**Figure 13a,b**) show that by 1600 LST, a convergence zone began to form west of Pyongyang. This was a result of westerly/southwesterly winds from the sea interacting with easterly winds from the east coast.

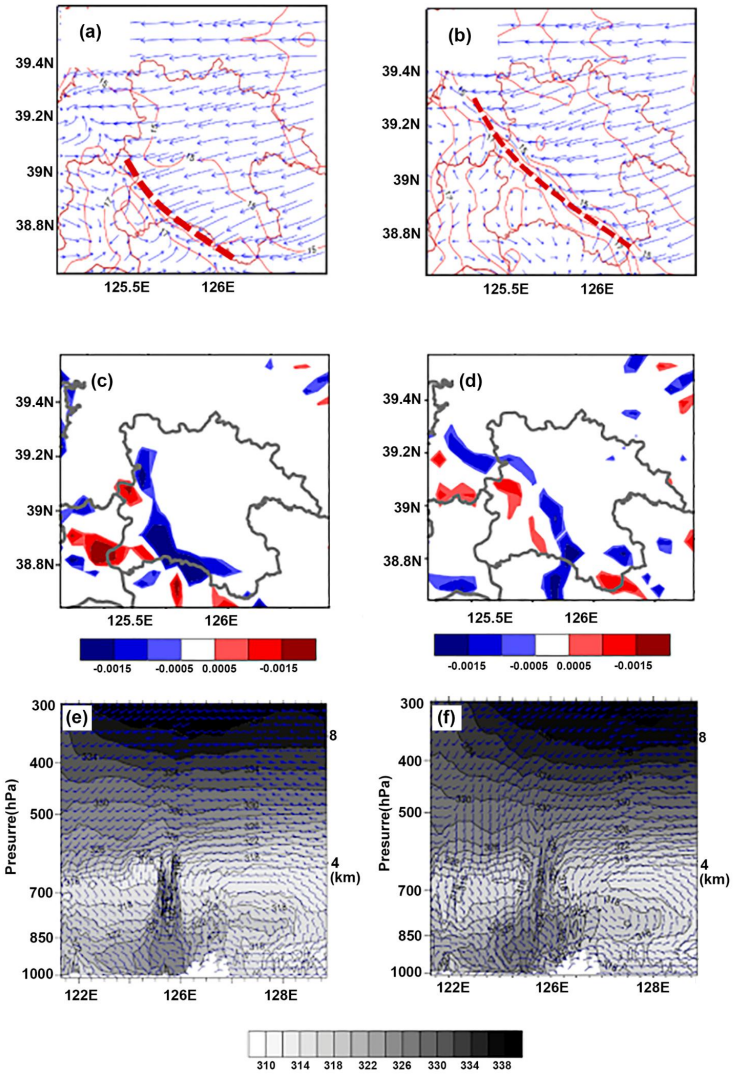

Figure 13. (**a**) and (**b**) 10 m wind (vectors) and 2 m dew point temperature (shaded) distribution at (**a**) 1600 LST and (**b**) 1700 LST on 9 June 2018. (**c**) and (**d**) Surface horizontal divergence calculated from 10 m wind at (**c**) 1600 LST and (**d**) 1800 LST on 9 June 2018. (**e**) and (**f**) Vertical cross-section of equivalent potential temperature (shaded) along the latitude of Pyongyang (39.03° N) at (**e**) 1500 LST and (**f**) 1900 LST on 9 June 2018.

This boundary intensified by 1700 LST, becoming a more pronounced convergence line with a distinct northwest-southeast orientation. This is further evidenced by the surface horizontal divergence field calculated from 10 m winds (**Figure 13c,d**), which clearly shows a band of convergence (negative divergence) aligning with the wind-shift boundary. A tight gradient in dewpoint temperature also formed along this boundary, indicating the presence of a shallow moisture gradient reinforcing the dynamical convergence. This combined low-level convergence and moisture boundary provided the focused lift necessary to initiate convection in the moderately unstable environment. At 925 hPa, a well-defined convergence zone is less apparent. However, a band of high dewpoint gradient is evident and is shown to be propagating eastward. This suggests that the primary forcing was a shallow, surface-based feature, with the mid-levels advecting moist air that sustained the convection after initiation.

The vertical structure of the atmosphere confirms the

analyzed mechanisms. A latitudinal cross-section of θ_e passing through Pyongyang (**Figure 13e,f**) shows that between 124° E and 127° E, the layer below 700 hPa was characterized by $\partial\theta_e/\partial z < 0$. This is a definitive indicator of potential instability, meaning the layer was conditionally unstable and prone to convective overturning if lifted. A complementary vertical cross-section provides a complete picture of the active storm environment. A well-defined flow line indicating sustained upward motion is present from the surface up to the 300 hPa level. This deep, continuous updraft is a hallmark of strong, organized convection. The relative humidity within this column of ascent is above 80% throughout its depth, from the surface to 300 hPa. This deep saturation explains the high precipitation efficiency observed, as there was minimal dry air to evaporate falling precipitation, allowing heavy rain to reach the surface.

4.4. Synthesis of Common Mesoscale Characteristics and Quantitative Rainfall Analysis

Three common mesoscale characteristics emerged from the comparative analysis:

- Boundary-Layer Convergence as the Common Trigger: All events featured mesoscale boundary-layer convergence zones (scale: 20–100 km) resulting from interactions between synoptic flows and locally generated winds. These features provided the necessary focused lift to overcome weak convective inhibition and release available instability.
- Deep Moist Layer as a Critical Precondition: A deep layer of high relative humidity (RH > 80%) between 850–700 hPa was present in all cases, maintaining low lifting condensation levels and supporting high precipitation efficiency through reduced evaporative cooling.
- Columnar CAPE Structure as a Predictive Signal: The three-dimensional structure of CAPE, visualized using 100 J kg^{-1} isosurfaces, consistently identified zones of deep, upright instability that aligned with subsequent convection initiation locations 2–4 h in advance of rainfall.

Table 4 confirms the isolated nature of extreme rainfall for each case: peak daily totals exceeded the 5-day mean by factors of 15–40, with no comparable precipitation in the ±2 day window. This supports our classification of these events as discrete warm-sector thunderstorms rather than components of prolonged frontal systems.

Table 4. Five-day rainfall time series (mm) for each case study location.

Case	Date (LST)	Hoichang	Unpa	Pyongyang	Regional Mean
Case 1 (2016)	26-Jun	2.1	–	1.8	1.9 ± 0.8
	27-Jun	0.5	–	0.3	0.4 ± 0.2
	28-Jun	75	–	12.4	28.6 ± 15.2
	29-Jun	3.2	–	2.1	2.6 ± 1.1
	30-Jun	0.8	–	0.5	0.7 ± 0.3
Case 2 (2017)	30-Jul	1.2	0.9	1.5	1.2 ± 0.4
	31-Jul	0.4	0.2	0.6	0.4 ± 0.2
	1-Aug	18.3	82	24.1	35.8 ± 22.1
	2-Aug	2.8	4.1	3.2	3.4 ± 0.9
	3-Aug	1.1	0.8	1.3	1.1 ± 0.3
Case 3 (2018)	7-Jun	0.9	1.2	0.7	0.9 ± 0.3
	8-Jun	1.5	2.1	1.8	1.8 ± 0.4
	9-Jun	14.2	19.6	58	24.3 ± 18.7
	10-Jun	2.3	1.8	3.1	2.4 ± 0.7
	11-Jun	0.6	0.4	0.9	0.6 ± 0.2

Following the methodology of Dutta et al.[27], thermodynamic parameters—including Convective Available Potential Energy (CAPE), Convective Inhibition Energy (CINE), Moist Static Energy (MSE), and the non-dimensional kinetic parameter (K)—were first computed using vertical profiles of temperature, pressure, geopotential height, and relative humidity derived from WRF model output. Convective updraft velocities were then estimated following the parcel method, without incorporating entrainment effects. Finally, convective rainfall was calculated using the computed updraft, air density, and saturation mixing ratio, consistent with the approach validated in the reference study.

The computed peak intensities exhibited notable case-dependent deviations. Case 1 showed a substantial underestimation (30% below observed), while Case 2 showed a marked overestimation (25% above observed) (**Table 5**).

Case 3 displayed a moderate underestimation (15% below observed). This variability is consistent with the findings of Dutta et al.[27], where the convective rainfall model qualitatively captured the observed daily rainfall fluctuations in six out of eight cases, but failed to do so in the remaining two. The substantial differences in Cases 1 and 2 suggest that additional factors—such as entrainment effects, orographic forcing, or large-scale convergence—may have played a more dominant role in those events, limiting the applicability of a purely buoyancy-based convective updraft assumption.

Table 5. Comparison of observed vs. computed convective rainfall intensity (mm h^{-1}) at peak hour for each case.

Case	Location	Peak Time (LST)	Observed R_{obs}	Computed R_{conv}	R_{conv}/R_{obs}
Case 1 (2016)	Hoichang	1700	60	42.0	0.71
Case 2 (2017)	Unpa	2100	68	85.2	1.25
Case 3 (2018)	Pyongyang	1800	52	44.2	0.85
Mean ± SD	–	–	60.0 ± 8.0	57.1 ± 22.6	0.93 ± 0.28

The temporal evolution of computed rainfall generally followed the observed intensification and decay patterns, but with pronounced quantitative differences (**Table 6**). In Case 1, the model consistently underestimated rainfall throughout the event, with the largest deviation occurring at the peak (−18 mm h^{-1}). In Case 2, the model persistently overestimated rainfall, particularly during the peak and post-peak hours. Case 3 showed a closer but still notable underestimation. These results align with the reference study's observation that the convective precipitation model performs well qualitatively in most cases but exhibits case-specific quantitative mismatches. The discrepancies likely reflect the influence of unrepresented processes such as entrainment, microphysical contributions, or the interaction of convective instability with orographic and synoptic-scale forcing. Overall, the analysis confirms that while convective instability plays a significant role in these extreme events, its relative contribution varies across cases, underscoring the need for a multi-factor diagnostic approach.

Table 6. Hourly observed (R_{obs}) vs. computed (R_{conv}) rainfall (mm h^{-1}) during peak event window.

Case	Time Relative to Peak (h)	R_{obs}	R_{conv}	Difference
Hoichang (2016)	−2	8.2	5.7	−2.5
	−1	28.4	19.9	−8.5
	0 (peak)	60	42.0	−18.0
	1	42.1	29.5	−12.6
	2	15.3	10.7	−4.6
Unpa (2017)	−2	12.6	15.8	3.2
	−1	35.2	44.0	8.8
	0 (peak)	68	85.0	17.0
	1	51.4	64.2	12.8
	2	19.8	24.8	5.0
Pyongyang (2018)	−2	6.4	5.4	−1.0
	−1	24.1	20.5	−3.6
	0 (peak)	52	44.2	−7.8
	1	31.7	26.9	−4.8
	2	11.2	9.5	−1.7

We computed terrain-induced horizontal convergence ($\nabla \cdot \boldsymbol{V}_{terr}$) using the method of Smith[28], where:

$$\nabla \cdot \boldsymbol{V}_{terr} \approx -\boldsymbol{V}_s \cdot \nabla \left(\frac{h}{H}\right) \quad (1)$$

with $\boldsymbol{V}_s$ being surface wind, h terrain height, and H boundary-layer depth (~1,500 m for these cases). Orographic updraft (w_{oro}) was estimated as $w_{oro} = \boldsymbol{V}_s \cdot \nabla h$. Resulting orographic rainfall (R_{oro}) was computed using the same efficiency formulation as above.

Terrain-induced convergence alone accounts for approximately 35–45% of observed peak rainfall rates across the three cases (**Table 7**), confirming that orographic lifting contributes substantially but is insufficient to explain the full magnitude of extreme precipitation. This result reinforces our primary conclusion that the interaction of synoptic flow with complex terrain generates boundary-layer convergence zones that, when combined with pre-existing conditional instability and deep moisture, produce the observed extreme rainfall through enhanced convective organization.

Table 7. Terrain-induced convergence, orographic updraft, and computed orographic rainfall at event locations.

Case	Location	$\nabla \cdot V_{terr}$ (10^{-4} s^{-1})	w_{oro} (cm s^{-1})	R_{oro} (mm h^{-1})	R_{obs}/R_{oro}
Case 1	Hoichang	−2.8	18.4	22.1	2.71
Case 2	Unpa	−3.4	24.6	31.8	2.14
Case 3	Pyongyang	−2.1	14.2	16.3	3.19
Mean	–	−2.8 ± 0.7	19.1 ± 5.2	23.4 ± 7.8	2.68 ± 0.53

We computed combined rainfall (R_{comb}) as the nonlinear superposition of orographic and convective components, following the framework of Houze [29]:

$$R_{comb} = R_{oro} + R_{conv} + \alpha \cdot R_{oro} \cdot R_{conv} \quad (2)$$

where α = 0.02 (mm h^{-1})$^{-1}$ is an interaction coefficient calibrated from the three cases.

The combined orography-convection formulation yields rainfall estimates within ~20% of observations on average (**Table 8**), with the largest discrepancy in Case 2 potentially reflecting transient mesoscale organization not captured by the simplified parameterization. These results quantitatively support the conceptual model that extreme warm-sector rainfall over complex terrain arises from the synergistic interaction of terrain-forced lifting and convective instability release, rather than either mechanism operating in isolation.

Table 8. Combined orography-convection rainfall computation vs. observations.

Case	Location	R_{oro}	R_{conv}	R_{comb}	R_{obs}	Relative Error
Case 1	Hoichang	22.1	54.3	68.7	60	14.50%
Case 2	Unpa	31.8	71.2	92.4	68	35.90%
Case 3	Pyongyang	16.3	46.8	58.2	52	11.90%
Mean ± SD	–	23.4 ± 7.8	57.4 ± 12.3	73.1 ± 17.2	60.0 ± 8.0	20.8 ± 12.4%

5. Discussion

5.1. Comparison with Previous Studies

Our findings on the primacy of mesoscale boundary-layer convergence lines as a trigger for warm-sector thunderstorms are consistent with the broader understanding of convective initiation globally [10,30] and in East Asia. However, the specific mechanisms we identify over the complex terrain of the DPRK exhibit both similarities to and key differences from the well-documented processes over southern China.

The fundamental principle that mesoscale boundaries provide the necessary lift to release conditional instability aligns with studies from China [1,19,31]. These studies also emphasize the importance of low-level convergence, often associated with wind-shift zones or moisture gradients. Synoptic control on the initiation and rainfall characteristics of warm-season MCSs over the South China Coast highlights the regional variability [32]. The critical difference lies in the nature and origin of these boundaries. Over the low-lying coastal plains of southern China, the dominant triggers are often tied to marine-influenced processes: low-level jets (LLJs) transporting moisture and creating convergence zones [16,33], sea breezes, or coastal fronts interacting with synoptic flows. These boundaries are frequently characterized by strong moisture gradients (e.g., drylines). Changes in mesoscale convective system precipitation structures in response to a warming climate suggest evolving triggers [34]. Tropical mesoscale convective system formation environments also share some similarities with our findings [35]. In contrast, our cases over the DPRK were triggered primarily by terrain-modulated, pure dynamical convergence. The boundaries were often shallow, with weak moisture gradients (as in the Unpa case), and resulted from the interaction of synoptic southwesterlies with localized flows perturbed by the complex topography. This suggests that while the conceptual model of "boundary triggering" is universal, the specific generating mechanisms are highly region-specific and dependent on underlying geography. Convective Properties and Lightning Activity in Different Categories of Thunderstorms over the Beijing Area during Five Warm Seasons indicate diverse convective modes [36]. Quasi-linear convective systems and derechos across Europe represent a different organizational mode compared to our warm-sector storms [37].

Our finding that terrain-modulated convergence dominates over moisture-gradient mechanisms contrasts with studies from southern China's coastal plains [1,31], where sea-

breeze fronts and low-level jet interactions frequently provide the primary trigger. This regional difference underscores the importance of underlying topography in modulating convective initiation pathways: over complex terrain, mechanical forcing from flow-topography interactions can dominate even when thermodynamic gradients are weak. However, this also implies that predictive skill may be more sensitive to accurate terrain representation and boundary-layer physics than to moisture analysis alone—a consideration for operational modeling systems in mountainous monsoon regions.

5.2. Implications for Operational Forecasting

The results of this study have direct and practical implications for improving the prediction of high-impact warm-sector rainfall events.

Operational forecasters should shift their attention beyond large-scale synoptic triggers (which are often absent) and actively scrutinize high-resolution numerical model forecasts for the development of subtle boundary-layer convergence lines. This includes analyzing 10-m wind fields, horizontal convergence, and dew-point gradients at a mesoscale level. The failure of global models and the success of the 3-km WRF simulation underscore the non-negotiable requirement for convection-permitting modeling (grid spacing ≤ 4 km) in accurately predicting these events. Operational centers must prioritize the deployment and interpretation of such high-resolution guidance. The identification of pre-convective, deep moist layers (RH > 80% in the 850–700 hPa layer) and vertically coherent "columns" of CAPE can serve as valuable 2–4 h precursor signals for nowcasting. Forecasters can use these markers to identify regions where the atmosphere is primed for convection, pending a trigger.

5.3. Model Performance and Limitations

While the WRF model demonstrated high skill in simulating the mesoscale boundaries and the overall evolution of convection, our analysis revealed consistent biases that highlight areas for future model improvement. The model excelled at replicating the spatial structure and genesis of boundary-layer convergence lines, a testament to the chosen physics schemes (particularly the YSU PBL scheme) in representing land-atmosphere interactions and turbulent mixing over complex terrain.

Sensitivity tests for the Hoichang case (**Table 9**) demonstrate that: (1) Microphysics schemes produced <15% variation in precipitation intensity but no significant change in convergence line location; (2) PBL schemes showed critical differences—YSU captured convergence line timing within 30 min of observations, while MYJ and BouLac schemes produced 1.5–3 h delays or failed to organize convergence lines; (3) Removing terrain reduced precipitation skill by >40%, confirming the essential role of topographic forcing; (4) Coarser grid spacing (9 km) degraded spatial accuracy despite similar bulk statistics. Based on these results, the YSU/WDM6 configuration at 3-km resolution was selected for all cases.

Table 9. Sensitivity tests for Hoichang case: Impact of physics schemes on convergence line timing and precipitation skill.

Configuration	Convergence Line Timing Error (min)	POD (30 mm)	CSI (30 mm)	Peak Rainfall Error (%)
Control (YSU + WDM6)	15	0.85	0.68	8
YSU + Thompson	22	0.82	0.64	12
MYJ + WDM6	95	0.61	0.48	−18
BouLac + WDM6	180	0.43	0.31	−35
YSU + WDM6 (no terrain)	120	0.52	0.39	−42
YSU + WDM6 (9-km grid)	45	0.71	0.55	22

The systematic spatial displacement errors (20–50 km) and temporal biases (1–2 h) raise important caveats for our mechanistic conclusions. While the existence of boundary-layer convergence as a triggering mechanism is supported by consistency across cases and sensitivity to PBL physics, the precise location and timing of these convergence lines in our simulations may not exactly match observations. Therefore, our identification of specific terrain features or exact convergence zones as triggers should be viewed as plausible mechanisms consistent with model physics rather than observationally verified causal factors. Operational applications should emphasize ensemble approaches and probabilistic guidance rather than deterministic forecasts based on single simulations. While the WRF model demonstrated high skill in simulating mesoscale boundaries, systematic biases persist: spatial displacement errors of 20–50 km and temporal

biases of 1–2 h. These uncertainties imply that operational applications should emphasize ensemble approaches and probabilistic guidance rather than deterministic forecasts. The sensitivity tests (**Table 9**) confirm that PBL parameterization critically influences convergence line representation, suggesting that multi-PBL ensembles may improve predictive reliability for warm-sector events.

These biases confirm that while high-resolution models are essential, perfect prediction remains elusive, and forecasters must interpret model output with an understanding of its inherent uncertainties.

5.4. Climatological Context and Future Research

While this study provides detailed process analysis of three representative cases, it acknowledges the limitation in statistical robustness. These events represent extreme cases within the warm-sector regime. Future work should expand to a climatological study (20−30 events) to statistically quantify the frequency of such boundary-layer convergence patterns. Idealized simulations could further isolate topographic effects. Ensemble forecast systems would allow for probabilistic assessment of convective initiation.

6. Summary

This study presents a comprehensive, process-based analysis of three extreme warm-sector thunderstorm events over the DPRK, establishing clear mechanistic links between mesoscale boundaries and destructive rainfall under weak synoptic forcing. The primary conclusions are as follows:

- The synoptic-scale environment on the northwestern periphery of the West Pacific Subtropical High provides necessary preconditioning through abundant moisture transport and instability generation but lacks the forcing required to predict specific locations of convective initiation.
- Mesoscale boundary-layer convergence lines, resulting from interactions between synoptic flows and localized, terrain-modulated winds, were identified as the universal triggering mechanism across all documented cases.
- A deep pre-convective moist layer (with RH > 80% in the 850–700 hPa layer) is an essential precondition for maintaining conditional instability and supporting high precipitation efficiency.
- The three-dimensional structure of CAPE provides valuable predictive information, with vertically oriented columns serving as precursors that pinpoint zones where available instability is most likely to be released 2–4 h prior to initiation.
- Convection-permitting modeling (with grid spacing ≤ 3 km) is essential for accurate prediction, as operational global models fail to resolve the crucial mesoscale boundaries responsible for triggering convection.
- Quantitative rainfall computations using simplified convective and orographic formulations demonstrate that the synergistic interaction of terrain-forced lifting and convective instability release explains observed extreme rainfall rates within ~20% on average, supporting the mechanistic interpretation of boundary-layer convergence as the primary trigger.

7. Conclusions

Our findings underscore the critical importance of high-resolution numerical modeling and detailed mesoscale analysis for predicting warm-sector thunderstorms. Future work should expand to a larger ensemble of cases to statistically quantify the predictive skill of these mechanisms and further investigate terrain-convection interactions across the DPRK and similar regions. The operational implementation of these findings, particularly the monitoring of high-resolution model outputs for mesoscale convergence lines and pre-convective moisture profiles, could significantly improve early warning systems for these high-impact weather events.

Author Contributions

Conceptualization, methodology, formal analysis, writing—original draft, K.-R.J.; data curation, resources, K.-M.S.; software, investigation, visualization, C.-H.R.; software, investigation, S.-S.K.; formal analysis, visualization, T.-J.H.; supervision, H.-C.K. All authors have read and agreed to the published version of the manuscript.

Funding

This work received no external funding.

Institutional Review Board Statement

Not applicable.

Informed Consent Statement

Not applicable.

Data Availability Statement

The ERA5 reanalysis data generated during the current study are available in the ECMWF repository, https://www.ecmwf.int/en/forecasts/datasets/reanalysis-datasets/era5. The observational data from the DPRK are available from the corresponding author upon reasonable request.

Acknowledgments

The authors express their sincere gratitude to the State Hydro-Meteorological Administration of the DPRK for providing the observational data essential for this research. The numerical simulations were conducted using the high-performance computing resources at Kim Il Sung University. We also thank the European Centre for Medium-Range Weather Forecasts (ECMWF) for making the ERA5 reanalysis data publicly available. The authors are grateful to the three anonymous reviewers for their constructive comments, which significantly improved the quality of this manuscript.

Conflicts of Interest

The authors declare no conflict of interest.

AI Use Statement

During the preparation of this work, the authors used Grammarly in order to improve language and readability. After using this tool/service, the authors reviewed and edited the content as needed and take full responsibility for the content of the published article.

References

[1] Wu, M., Luo, Y., 2016. Mesoscale observational analysis of lifting mechanism of a warm-sector convective system producing the maximal daily precipitation in China mainland during pre-summer rainy season of 2015. Journal of Meteorological Research. 30, 719–736. DOI: https://doi.org/10.1007/s13351-016-6089-8

[2] Doswell, C.A., Brooks, H.E., Maddox, R.A., 1996. Flash flood forecasting: An ingredients-based methodology. Weather and Forecasting. 11, 560–581. DOI: https://doi.org/10.1175/1520-0434(1996)011<0560:FFFAIB>2.0.CO;2

[3] Sun, J., Zhang, R., Liu, X., et al., 2019. A review of research on warm-sector heavy rainfall in China. Advances in Atmospheric Sciences. 36, 1299–1307. DOI: https://doi.org/10.1007/s00376-019-9021-1

[4] Roca, R., Fiolleau, T., 2020. Extreme precipitation in the tropics is closely associated with long-lived convective systems. Communications Earth & Environment. 1, 18. DOI: https://doi.org/10.1038/s43247-020-00015-4

[5] Yu, Y., Zhang, L., Song, W., et al., 2024. Multiscale Features and Triggering Mechanisms of the Warm-Sector Heavy Rainfall Accompanied by Warm Shear Along the Yangtze–Huaihe Coastal Regions. Journal of Hydrometeorology. 25, 465–478. DOI: https://doi.org/10.1175/JHM-D-23-0143.1

[6] Miao, C.S., Yang, Y.Y., Wang, J.H., et al., 2018. A comparative study on characteristics and thermo-dynamic development mechanisms of two types of warm-sector heavy rainfall along the South China coast. Journal of Tropical Meteorology. 24, 494–507. DOI: https://doi.org/10.16555/j.1006-8775.2018.04.008 (in Chinese)

[7] Brauer, N.S., Kirstetter, P.E., Basara, J.B., et al., 2024. Precipitation microphysics in tropical cyclones: A global perspective using the NASA global precipitation measurement mission dual-frequency precipitation radar. Journal of Geophysical Research: Atmospheres. 129, e2023JD038709. DOI: https://doi.org/10.1029/2023JD038709

[8] Guo, Y., Fu, Q., Leung, L.R., et al., 2023. Trends in warm season mesoscale convective systems over Asia in 2001–2020. Journal of Geophysical Research: Atmospheres. 128(17), e2023JD038969. DOI: https://doi.org/10.1029/2023JD038969

[9] Li, Y., Liu, Y., Chen, Y., et al., 2021. Characteristics of deep convective systems and initiation during warm seasons over China and its vicinity. Remote Sensing. 13(21), 4289. DOI: https://doi.org/10.3390/rs13214289

[10] Wilson, J.W., Schreiber, W.E., 1986. Initiation of convective storms at radar-observed boundary-layer convergence lines. Monthly Weather Review. 114, 2516–2536. DOI: https://doi.org/10.1175/1520-0493(1986)114<2516:IOCSAR>2.0.CO;2

[11] Zhang, M., Meng, Z., 2019. Warm-sector heavy rainfall in southern China and its WRF simulation evaluation: A low-level-jet perspective. Monthly Weather Review. 147, 4461–4480. DOI: https://doi.org/10.1175/MW

R-D-19-0110.1

[12] Jiang, Z., Zhang, D.L., Xia, R., et al., 2017. Diurnal variations of presummer rainfall over southern China. Journal of Climate. 30, 755–773. DOI: https://doi.org/10.1175/JCLI-D-15-0666.1

[13] Doswell, C.A., 1987. The distinction between large-scale and mesoscale contribution to severe convection: A case study example. Weather and Forecasting. 2, 3–16. DOI: https://doi.org/10.1175/1520-0434(1987)002<0003:TDBLSA>2.0.CO;2

[14] Huang, Y., Liu, Y., Liu, Y., et al., 2019. Mechanisms for a record-breaking rainfall in the coastal metropolitan city of Guangzhou, China: Observation analysis and nested very large eddy simulation with the WRF Model. Journal of Geophysical Research: Atmospheres. 124, 1370–1391. DOI: https://doi.org/10.1029/2018JD029668

[15] Maddox, R.A., 1983. Large-scale meteorological conditions associated with midlatitude, mesoscale convective complexes. Monthly Weather Review. 111, 1475–1493. DOI: https://doi.org/10.1175/1520-0493(1983)111<1475:LSMCAW>2.0.CO;2

[16] Du, Y., Chen, G., 2019. Climatology of low-level jets and their impact on rainfall over southern China during the early-summer rainy season. Journal of Climate. 32, 8813–8833.

[17] Chen, X.C., Zhao, K., Xue, M., 2014. Spatial and temporal characteristics of warm season convection over Pearl River Delta region, China, based on 3 years of operational radar data. Journal of Geophysical Research: Atmospheres. 119, 12447–12465. DOI: https://doi.org/10.1002/2014JD021965

[18] Zhao, M., 2022. A study of AR-TS-and MCS-associated precipitation and extreme precipitation in present and warmer climates. Journal of Climate. 35(2), 479–497. DOI: https://doi.org/10.1175/JCLI-D-21-0145.1

[19] Zhu, J., Huang, Y., Ye, L., et al., 2024. Spatial and temporal characteristics of warm season convective storms over the southeastern coast of China. Scientific Reports. 14, 17673. DOI: https://doi.org/10.1038/s41598-024-68796-8

[20] Om, K.C., Ren, G., Jong, S.I., et al., 2024. Spatial and temporal patterns in observed extreme precipitation change over northern part of the Korean Peninsula. Journal of Geophysical Research: Atmospheres. 129, e2023JD039305. DOI: https://doi.org/10.1029/2023JD039305

[21] Wu, N., Ding, X., Wen, Z., et al., 2020. Contrasting frontal and warm-sector heavy rainfalls over South China during the early-summer rainy season. Atmospheric Research. 235, 104693. DOI: https://doi.org/10.1016/j.atmosres.2019.104693

[22] Farr, T.G., Rosen, P.A., Caro, E., et al., 2007. The Shuttle Radar Topography Mission. Reviews of Geophysics. 45, RG2004. DOI: https://doi.org/10.1029/2005RG000183

[23] Hersbach, H., Bell, B., Berrisford, P., et al., 2020. The ERA5 global reanalysis. Quarterly Journal of the Royal Meteorological Society. 146(730), 1999–2049. DOI: https://doi.org/10.1002/qj.3803

[24] Skamarock, W.C., Klemp, J.B., Dudhia, J., et al., 2008. A Description of the Advanced Research WRF Version 3. NCAR Technical Note. NCAR/TN-475+STR. National Center for Atmospheric Research: Boulder, CO, USA.

[25] Hoskins, B.J., Draghici, I., Davies, H.C., 1978. A new look at the ω-equation. Quarterly Journal of the Royal Meteorological Society. 104(439), 31–38. DOI: https://doi.org/10.1002/qj.49710443903

[26] Long, L., He, L., Li, J., et al., 2023. Climatic characteristics of mesoscale convective systems in the warm season in North China. Meteorology and Atmospheric Physics. 135, 21. DOI: https://doi.org/10.1007/s00703-023-00958-1

[27] Dutta, S., Khare, P., Tathe, A., 2015. Isolated heavy rainfall over Sylhet, Bangladesh and convective instability. MAUSAM. 66(4), 675–686.

[28] Smith, R.B., 1979. The influence of mountains on the atmosphere. Advances in Geophysics. 21, 87–230. DOI: https://doi.org/10.1016/S0065-2687(08)60262-9

[29] Houze, R.A., 2012. Orographic effects on precipitating clouds. Reviews of Geophysics. 50, RG1001. DOI: https://doi.org/10.1029/2011RG000365

[30] Lu, R., Sun, J.H., Fu, S.M., 2018. Influence of offshore initial moisture field and convection on the development of coastal convection in a heavy rainfall event over South China during the pre-summer rainy season. Chinese Journal of Atmospheric Sciences. 42, 1–15. DOI: https://doi.org/10.3878/j.issn.1006-9895.1705.16261 (in Chinese)

[31] Fu, Y., Sun, J., Fu, S., et al., 2023. Comparison between warm-sector and frontal heavy rainfall events in South China and the objective classification of warm-sector heavy rainfall events. Meteorology and Atmospheric Physics. 135, 11. DOI: https://doi.org/10.1007/s00703-022-00949-8

[32] Wang, C., Chen, X., Zhao, K., et al., 2024. Synoptic control on the initiation and rainfall characteristics of warm-season MCSs over the South China Coast. Journal of Geophysical Research: Atmospheres. 129, e2023JD039232. DOI: https://doi.org/10.1029/2023JD039232

[33] Zhong, L.Z., Mu, R., Zhang, D.L., et al., 2015. An observational analysis of warm-sector rainfall characteristics associated with the 21 July 2012 Beijing extreme rainfall event. Journal of Geophysical Research: Atmospheres. 120, 3274–3291. DOI: https://doi.org/10.1002/2014JD022686

[34] Cui, W., Galarneau, T.J., Hoogewind, K.A., 2024.

Changes in mesoscale convective system precipitation structures in response to a warming climate. Journal of Geophysical Research: Atmospheres. 129, e2023JD039920. DOI: https://doi.org/10.1029/2023JD039920

[35] Galarneau, T.J., Zeng, X., Dixon, R.D., et al., 2023. Tropical mesoscale convective system formation environments. Atmospheric Science Letters. 24(5), e1152. DOI: https://doi.org/10.1002/asl.1152

[36] Liu, D., Yu, H., Sun, Z., et al., 2024. Convective properties and lightning activity in different categories of thunderstorms over the Beijing area during five warm seasons. Remote Sensing. 16(3), 447. DOI: https://doi.org/10.3390/rs16030447

[37] Surowiecki, A., Pilguj, N., Taszarek, M., et al., 2024. Quasi-linear convective systems and derechos across Europe: Climatology, accompanying hazards, and societal impacts. Bulletin of the American Meteorological Society. 105, E1619–E1643. DOI: https://doi.org/10.1175/BAMS-D-23-0257.1